Petroleum Science 23 (2026) 2175–2187

Contents lists available at ScienceDirect

Petroleum Science

journal homepage: www.keaipublishing.com/en/journals/petroleum-science

Original Paper

Mechanical characteristic and damage mechanism of carbon/glass composites in offshore oil exploration

Yan-Wen Zhang [a,b], Yu-Jing Chen [a], Jia-Qi Che [c,*], Yu-Feng Jiang [a,b], Wen-Cheng Liu [a,b], Xin-Fu Liu [d]

[a] College of Engineering, Ocean University of China, Qingdao, 266404, Shandong, China
[b] State Key Laboratory of Coastal and Offshore Engineering, Ocean University of China, Qingdao, 266100, Shandong, China
[c] College of Mechanical and Electronic Engineering, China University of Petroleum (East China), Qingdao, 266580, Shandong, China
[d] College of Mechanical and Automotive Engineering, Qingdao University of Technology, Qingdao, 266520, Shandong, China

ARTICLE INFO

Article history:
Received 13 September 2024
Received in revised form
7 April 2025
Accepted 16 November 2025
Available online 20 November 2025

Edited by Teng Zhu and Min Li

Keywords:
Carbon/glass hybrid rod
Constitutive model
Stress distribution rule
Progressive damage

ABSTRACT

Carbon/glass hybrid rods exhibit superior tensile strength, low weight, and exceptional corrosion resistance. However, rod splitting presents a considerable challenge to their practical applications, impeding widespread acceptance. A strength prediction model for carbon/glass hybrid rods was created utilizing a multi-mode damage constitutive material model. Tensile experiments were conducted to validate the simulation model, elucidating stress distribution patterns and creating progressive damage evolution laws to clarify failure causes, thus offering theoretical support for the construction of high-strength rods. The results indicated that: (1) Experimental data indicated an average tensile load of 452.4 kN, with failure resulting from brittle fracture and interface debonding; (2) The simulated ultimate tensile load was 439.2 kN, deviating by 3% from experimental values within acceptable engineering accuracy limits; (3) As displacement increased from 0.3 mm to 0.7 mm, von Mises stresses in the coating layer, −40° winding layer, 40° winding layer, and core layer rose from 96.4, 62.2, 43.6, and 199.2 MPa to 229.6, 141.6, 111.1, and 472.4 MPa, respectively; (4) The primary forms of damage were interface debonding, matrix cracking, matrix extrusion, fiber extrusion and fiber fracture. The weak interface strength and asynchronous deformation between the carbon-fiber core layer and the glass-fiber cladding layer facilitated interface slip, leading to the premature failure of the winding layer due to a rapid decline in interface load transfer, ultimately resulting in interlayer splitting failure of the rod.

1. Introduction

The advancement of offshore oil and gas resources is essential for maintaining national energy security. The steel rod, a crucial component in offshore rod pumping, has drawbacks such as high density, insufficient corrosion resistance, and accelerated wear rates (Betts et al., 2019; Qi et al., 2023; Du et al., 2024). Conversely, carbon/glass hybrid rods possess characteristics such as low weight, high strength, corrosion resistance, and fatigue resistance, enabling them to endure high-frequency reciprocating motions in harsh downhole conditions, leading to a 70% weight reduction compared to steel rods (Bai et al., 1997; Bek et al., 2021). However, the field investigation found rod splitting which greatly hinders the widespread application of carbon/glass hybrid rods. Therefore, it is urgent to study the physical characteristics and damage mechanisms to provide theoretical guidance for carbon/glass hybrid rods.

Carbon/glass hybrid rods were initially created in the early 1980s. They were successfully developed in the early 1990s after nearly ten years of research and development, utilizing specialized operating equipment and software to integrate carbon/glass hybrid rods with steel rods (Akpinar and Aydin, 2014; Yan and Cao, 2018). The company utilized carbon/glass hybrid rods in 33 pumping wells from 1991 to 1995 to evaluate their practicality. The average pump depth was 1444 m, the average pump diameter was 50.5 m, the length of the carbon/glass hybrid rod constituted 56.8%, the average bottom hole temperature was 42.7 °C, and the average pump diameter was 50.5 m. Over a period of four years, 45

* Corresponding author.
E-mail address: cjqupc@163.com (J.-Q. Che).
Peer review under the responsibility of China University of Petroleum (Beijing).

https://doi.org/10.1016/j.petsci.2025.11.029

tests were administered across 33 wells. The principal failure mechanisms were rod splitting and joint fracture (Biscaia et al., 2016; Hasheminia et al., 2019). At the same time, Russia and Sweden have created a rectangular flexible rod that can be coiled and packaged without any connections. However, the flexible rod can only be used for non-corrosion resistant and self-supporting oil wells, with depths ranging from 1000 to 3000 m (Cox et al., 2019; Kupski et al., 2019). Delmonte et al. conducted fatigue experiments to assess the residual strength of several rods. The analysis indicated that the residual strength of glass hybrid rods was 20%, steel rods had a residual strength of 40%, and carbon/glass hybrid rods exhibited a remarkable residual strength of 90% (Delmonte, 1987). Feng et al. studied the effect of process parameters on the mechanical and fatigue properties of carbon/glass hybrid rods. The results showed that the hybrid rod has the characteristics of light weight, high strength, and fatigue resistance, making it suitable for application in deep-well reservoirs (Feng et al., 2021). Xian et al. revealed the influence mechanism of different soaking temperature, liquid pressure and salt solution concentration on the water absorption performance of carbon/glass composite sucker rod. The findings indicated that the longitudinal sucker rod had a lower water absorption rate and a higher diffusion coefficient compared to the radial sucker rod (Xian et al., 2024). Menshykova et al. investigated the degradation resulting from repeated bending loads on hybrid rods by bending strain tests to assess the bending behavior of the hybrid rod under varying creep durations (Menshykova et al., 2014; Malmorad et al., 2020). Firouzsalari et al. investigated the effects of temperature and water absorption on the interfacial mechanical characteristics of carbon/glass hybrid rods. With increasing temperatures, the fracture process transitioned from brittle to ductile (Doitrand et al., 2015; Firouzsalari et al., 2021; Hou et al., 2022; Al-Mahfooz and Mahdi, 2023; Wang et al., 2025). Karthik et al. studied the tensile-tension fatigue characteristics of carbon/glass hybrid rods consisting of unidirectional carbon-fiber cores and glass-fiber shells. It was found that progressive fatigue damage modes occurred at high stress ratios and low levels of stress variability (Karthik et al., 2022).

To summarize, both domestic and international experts have extensively studied the mechanical properties of hybrid rods. However, there is a limited amount of research available on the use of carbon/glass hybrid rods in offshore oil and gas resources considering multi-mode damage modes. The failure mechanisms of fiber, matrix and interface at micro scale cannot be correlated with the residual strength of hybrid rods at macro scale. Hence, a material constitutive model for a carbon/glass hybrid rod was formulated, taking into account various factors such as fiber stretching, fiber extension, matrix cracking, matrix extension, and interfacial debonding. The dynamic damage analysis method for carbon/glass hybrid rods was proposed revealing the failure mechanism and damage evolution law under multi-mode damage effects.

2. Mechanics experiment

2.1. Specimens structure

Carbon/glass hybrid rods produced by Shengli Xinda Composite Co., LTD. are manufactured using the pultrusion process. The raw materials used include carbon fiber, glass fiber and bisphenol A type epoxy resin, in which the fiber volume fraction is approximately 70%. Among them, the middle layer consists of two layers of glass fiber reinforced polymer (GFRP) wound at a 40° angle. The shape of the external/core interface of carbon/glass hybrid rod is irregular, approximately circular, which increases the interlayer adhesion. The morphology of carbon/glass hybrid rod is shown in Fig. 1 (Zhang et al., 2024a,b).

2.2. Experimental design

According to GB/T 13096–2008 “Test method for mechanical properties of pultruded glass fiber reinforced plastic rod” and Q/SXD 025–2017 “Enterprise Standard of Shengli Oilfield Xinda Pipe Technology Development Co., LTD.”, carbon/glass hybrid rods with a diameter of 22 mm, a length of 600 mm. The experimental setup utilized a WAW-1000F microcomputer-controlled electro-hydraulic servo universal testing system equipped with digital closed-loop control. Hydraulically actuated wedge grips were employed at both clamping ends to prevent localized crushing damage. Axial tensile loading was applied under displacement control at a constant crosshead speed of 5.0 mm/min. Testing proceeded until complete specimen failure characterized by longitudinal matrix splitting and fiber bundle separation. Load-displacement data were recorded until specimen rupture. Post-test analysis included macroscopic fracture documentation using digital imaging and microscopic characterization through SEM (Scanning Electron Microscope) to differentiate failure mechanisms between carbon and glass fiber components (Zhang et al., 2026). Finally, 5 sets of valid test data meeting the requirements of the standard were selected, and the tensile strength of the rod was calculated by arithmetic average method, and the nonlinear characteristics of load-displacement curves and the consistency of failure modes were analyzed. The tensile test of the carbon/glass hybrid rod is shown in Fig. 2. The material parameters of hybrid rod supplied by the manufacturer.

3. Finite element model

3.1. Material constitutive model

(1) Fiber constitutive model

The Hashin criterion is used to simulate fiber stretching failure and fiber extrusion failure in composite materials (Zhang et al., 2024a,b).

Fiber stretching damage factor f_t:

$$f_t = \left(\frac{\sigma_{11}}{X_T}\right)^2 + \left(\frac{\tau_{12}}{S_{12}}\right)^2 + \left(\frac{\tau_{13}}{S_{13}}\right)^2 \geq 1 \tag{1}$$

In the formula, σ_{11} is normal stress vector, MPa; τ_{12}, τ_{12} is tangential stress vector, MPa.

Fiber extension damage factor f_c:

$$f_c = \left(\frac{\sigma_{11}}{X_C}\right)^2 \geq 1 \tag{2}$$

The initial fiber damage was determined according to Hashin damage criterion, and the bilinear degraded constitutive model based on energy evolution was adopted to analyze the influence of damage factors on property degradation. The bilinear degraded constitutive model is shown.

Fiber failure factor $d_{11}^{t,c}$:

$$d_{11}^{t,c} = \frac{\varepsilon_{11}^{f(t,c)}\left(\varepsilon_{11} - \varepsilon_{11}^{o(t,c)}\right)}{\varepsilon_{11}\left(\varepsilon_{11}^{f(t,c)} - \varepsilon_{11}^{o(t,c)}\right)} \tag{3}$$

in the formula, $\varepsilon_{11}^{f(t,c)}$ is fiber fracture strain, %; $\varepsilon_{11}^{o(t,c)}$ is initial damage strain, %.

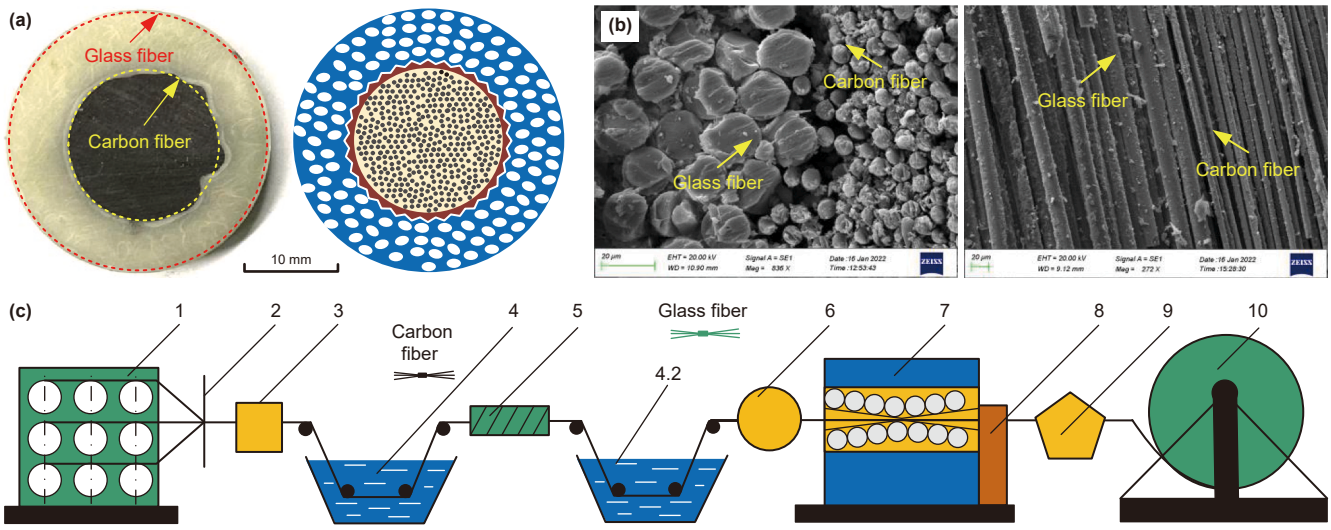

Fig. 1. Morphology of carbon/glass hybrid rod with **(a)** structure, **(b)** microstructure and **(c)** preparation. 1: wire rack; 2: preheating system; 3: fiber dipping area; 4: heating mold; 5: braiding machine; 6: pultrusion mold; 7: post-curing heating furnace; 8: traction device; 9: winding device.

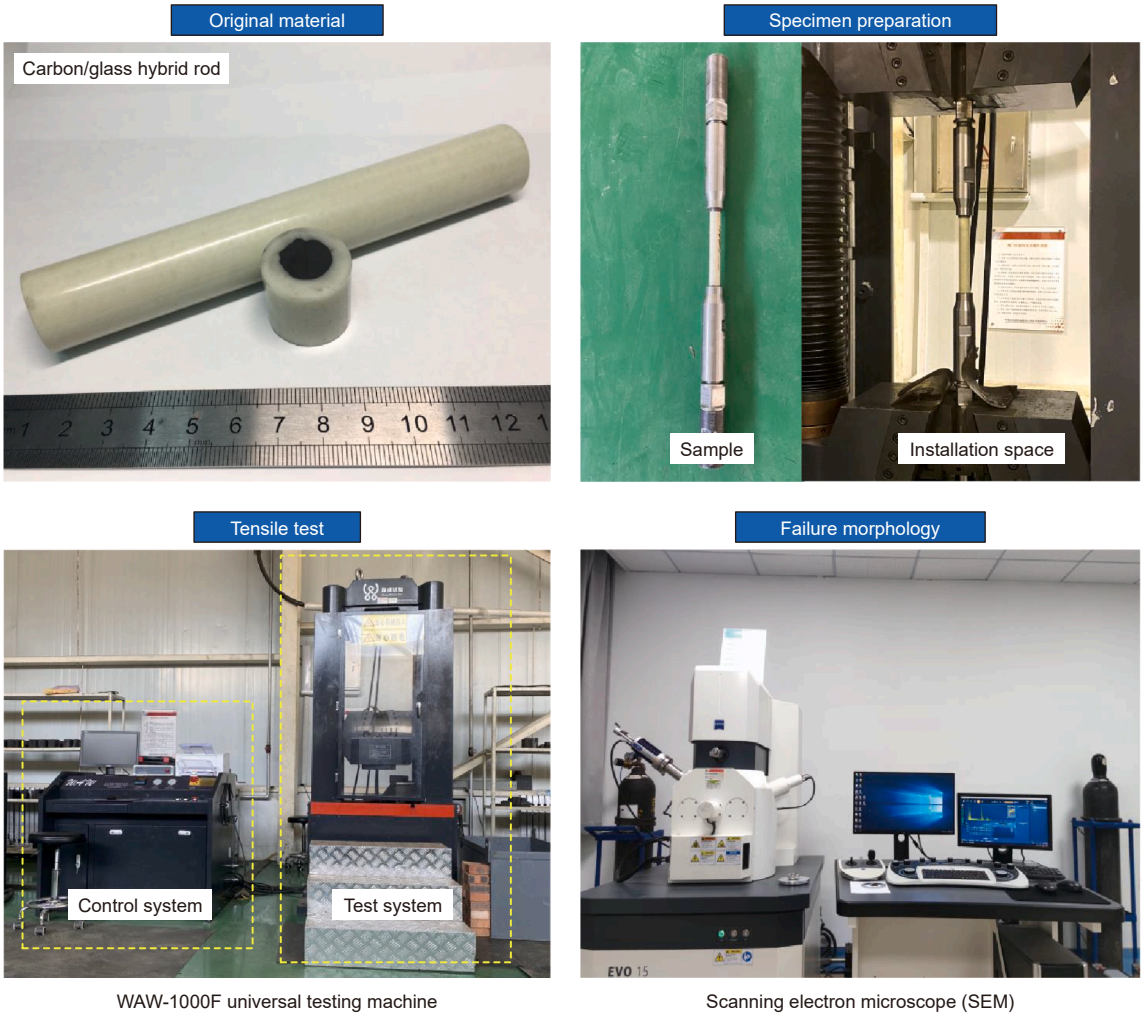

Fig. 2. Flow chart for tensile test of carbon/glass hybrid rod.

(2) Matrix constitutive model

The Puck criterion is used to simulate matrix separation cracks and matrix extrusion cracks in composite materials. In parallel with the fiber direction, there is the possibility of a fracture surface, and the crack angle θ is defined in direction 2. The failure criterion was determined by analyzing the stress on the surface of the fracture. The bilinear constitutive model of matrix fracture is shown.

Matrix cracking damage factor f_m^t ($\sigma_n \geq 0$):

$$f_m^t = \left[\left(\frac{1}{Y_T} - \frac{p_{\perp\psi}^t}{R_{\perp\psi}^A}\right)^2 \sigma_n(\theta)^2 + \left(\frac{\tau_{nt}(\theta)}{R_{\perp\perp}^A}\right)^2 + \left(\frac{\tau_{nl}(\theta)}{S_{12}}\right)^2\right]^{1/2} + \frac{p_{\perp\psi}^t}{R_{\perp\psi}^A}\sigma_n(\theta) \tag{4}$$

Matrix extension damage factor f_m^c ($\sigma_n < 0$):

$$f_m^c = \left[\left(\frac{p_{\perp\psi}^c}{R_{\perp\psi}^A}\right)^2 \sigma_n(\theta)^2 + \left(\frac{\tau_{nt}(\theta)}{R_{\perp\perp}^A}\right)^2 + \left(\frac{\tau_{nl}(\theta)}{S_{12}}\right)^2\right]^{1/2} + \frac{p_{\perp\psi}^c}{R_{\perp\psi}^A}\sigma_n(\theta) \tag{5}$$

Among them,

$$\frac{p_{\perp\psi}^t}{R_{\perp\psi}^A} = \frac{p_{\perp\perp}^t}{R_{\perp\perp}^A}\cos^2\psi + \frac{p_{\perp\parallel}^t}{S_{12}}\sin^2\psi, R_{\perp\perp}^A = \frac{Y_C}{2(1+p_{\perp\perp}^c)}, \cos^2\psi = \frac{\tau_{nt}^2(\theta)}{\tau_{nt}^2(\theta)+\tau_{nl}^2(\theta)}, \sin^2\psi = \frac{\tau_{nl}^2(\theta)}{\tau_{nt}^2(\theta)+\tau_{nl}^2(\theta)} \tag{6}$$

In the formula, τ_{nt} is stress perpendicular to the fiber direction, MPa; τ_{nl} is stress parallel to fiber direction, MPa; θ is fracture angle, °; $R_{\perp\perp}^A$ is fracture strength, MPa; $p_{\perp\perp}^t$, $p_{\perp\perp}^c$, $p_{\perp\parallel}^t$, $p_{\perp\parallel}^t$ is inclination parameter.

Equivalent failure strain ε_{eq}^m:

$$\varepsilon_{eq}^m = \frac{2}{L_C}\left[\left(\frac{\sigma_n^0\beta_n}{G_{2c}^k}\right)^2 + \left(\frac{\tau_{nl}^0\beta_{nl}}{G_{12c}}\right)^2 + \left(\frac{\tau_{nt}^0\beta_{nt}}{G_{23c}}\right)^2\right]^{-1/2} \tag{7}$$

Among them,

$$\sigma_n^0 = \frac{\sigma_n}{\left(f_m^{t,c}\right)^{1/2}}, \tau_{nl}^0 = \frac{\tau_{nl}}{\left(f_m^{t,c}\right)^{1/2}}, \tau_{nt}^0 = \frac{\tau_{nt}}{\left(f_m^{t,c}\right)^{1/2}}, \beta_n = \frac{\langle\varepsilon_n\rangle}{\varepsilon_{eq}}, \beta_{nl} = \frac{\varepsilon_{nl}}{\varepsilon_{eq}}, \beta_{nt} = \frac{\varepsilon_{nt}}{\varepsilon_{eq}} \tag{8}$$

Matrix fracture factor:

$$d = \frac{\varepsilon_{eq}^m}{\varepsilon_{eq}^m - \varepsilon_{eq}^0}\left(1 - \frac{\varepsilon_{eq}^0}{\varepsilon_{eq}}\right) \tag{9}$$

In the formula, $\varepsilon_{eq} = \sqrt{\langle\varepsilon_n\rangle^2 + \varepsilon_{nl}^2 + \varepsilon_{nt}^2}$ is element equivalent strain, $\langle\varepsilon_n\rangle = \max(0, \varepsilon_n)$, %; ε_{eq}^0 is equivalent initial damage strain, %; L_C is element feature length, mm; G_{2c}^k is critical fracture energy release rate when transversely stretched or compressed, N/mm; G_{12c}, G_{23c} is in-plane shear critical fracture energy release rate, N/mm.

(3) Interface constitutive model

The interface damage model adopts cohesive elements, which are combined with interface element. Crack propagation is simulated through the degradation of stiffness in interface elements. The constitutive model is expressed as follows:

$$\begin{Bmatrix}\sigma_n\\ \sigma_s\\ \sigma_t\end{Bmatrix} = \begin{bmatrix}K_{nn} & 0 & 0\\ 0 & K_{ss} & 0\\ 0 & 0 & K_{tt}\end{bmatrix}\begin{Bmatrix}\varepsilon_n\\ \varepsilon_s\\ \varepsilon_t\end{Bmatrix} \tag{10}$$

In the formula, K_{nn}, K_{ss} and K_{tt} represent the normal and tangential stiffness respectively, N/mm.

Based on the quadratic stress damage criterion, the initial damage of cohesive element was estimated. The expression is as follows:

$$\left[\frac{\sigma_n}{T_n}\right]^2 + \left[\frac{\tau_s}{T_s}\right]^2 + \left[\frac{\tau_t}{T_t}\right]^2 = 1 \tag{11}$$

In the formula, T_n, T_s, T_t represents the cohesive element strength in certain direction, MPa.

The failure judgment of interface elements is based on the Benzeggagh and Kenane (B-K) criterion of mixed damage modes. The formula of B-K criterion is as follows:

$$G_{IC} + (G_{IIC} - G_{IC})\left(\frac{G_S}{G_T}\right)^\eta = G_C \tag{12}$$

In the formula, G_{IC}, G_{IIC} are normal and tangential interface failure critical energy release rate, N/mm; $G_S = G_s + G_t$, $G_T = G_n + G_s + G_t$, G_n, G_s and G_t are normal and tangential interface energy release rate, N/mm. η is material softening index determined by test.

3.2. Numerical simulation model

By using ABAQUS simulation software, a finite element model of carbon/glass hybrid rods of 22 mm in diameter and 300 mm in length was developed along with explicit integration algorithms, using Hashin criterion, Puck criterion and cohesive model as failure criteria for fibers, matrixes, and interfaces. Among them, the carbon-fiber core layer, ±40° glass-fiber winding layer and glass-fiber coating layer adopted a three-dimensional reduced integration element C3D8R. The interface adopted three-dimensional COHED8 element. The carbon/glass hybrid rod was meshed using the scanning grid method combined with hourglass control and the neutral axis algorithm.

3.3. Constraints condition

The finite slip method was used to define the global constraints in the simulation model of carbon/glass hybrid rod. A hard contact constraint was set for the normal constraint. Tangential constraints were set as penalty functions with friction coefficients of 0.15. Global fixed constraints were applied to the left end of the coating layer. Moreover, the right end of the coating layer was displaced in the Z direction at a stretching speed of 5 mm/min, while all other directions were fixed. A finite element model of the carbon/glass hybrid rod is shown in Fig. 3.

4. Mechanical characteristics analysis

4.1. Load-displacement curve

According to the test procedure, the tensile strength tests of carbon/glass hybrid rods were carried out and the results are shown in Table 1. The carbon/glass hybrid rod was prone to splitting and fracturing. The average tensile load was 452.4 kN, with a corresponding axial displacement of 1.54 mm. The simulation model calculated the ultimate tensile load as 439.2 kN, with a corresponding axial displacement of 1.52 mm. The discrepancy

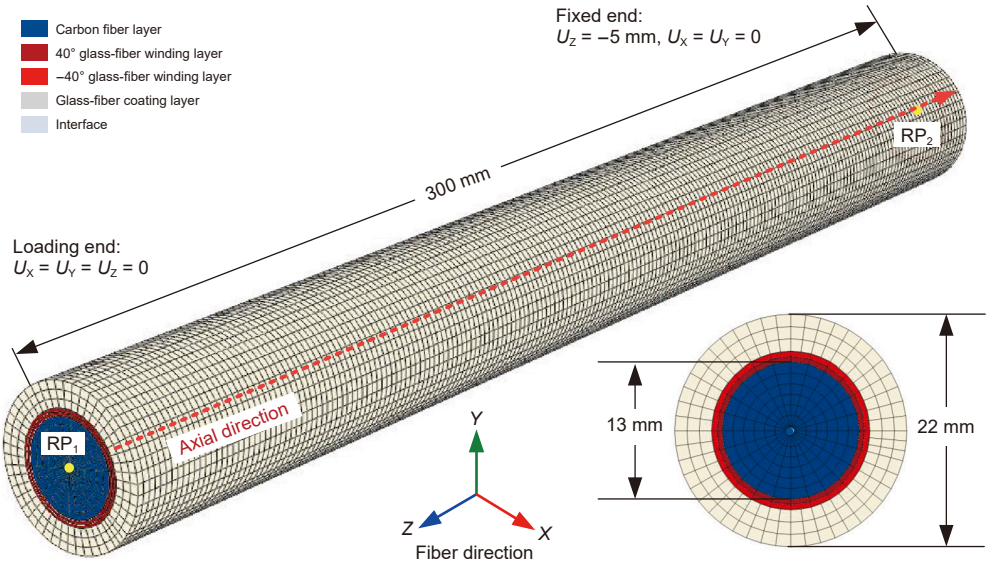

Fig. 3. Numerical simulation model of carbon/glass hybrid rod.

between the test results and the simulation results was 3%, caused by the initial asymmetrical error of the test model and the installation error of the test fixture. The simulation model yields lower values compared to the test results when subjected to the same displacement circumstance. The load-displacement curve of carbon/glass hybrid rod under tensile load is shown in Fig. 4.

According to the experimental results, there were four stages in the tensile curve of carbon/glass hybrid rods: fixture pre-tightening stage AB, linear elastic stage BC, damage evolution stage CD and failure splitting stage DE.

At the pre-tightening stage AB, as the tensile load increased to 36 kN, the tensile displacement also increased to 0.1 mm. The initial intermittent between the fixture and the carbon/glass hybrid rod was eliminated, and the carbon/glass hybrid rod was pre-tightened.

At the elastic deformation stage BC, as the tensile displacement increased within the range of 0.1 mm–0.7 mm, the tensile load increased linearly, and there was no obvious damage on the surface of the carbon/glass hybrid rod. At a displacement of 0.7 mm and the tensile load reached 211.0 kN, the specimen made a breaking sound. The glass-fiber coating layer near the fixture caused interface cracking and fiber breakage. Correspondingly, the load-displacement curve was slightly bent, indicating obvious damage on the surface of the glass-fiber coating layer.

At the damage evolution stage, as the tensile displacement increases within the range of 0.7–1.54 mm, the tensile curve showed continuous fluctuations, with the bending amplitude constantly increasing, accompanied by a sharp splitting sound. At the same time, cracks appeared near the fixture and propagated perpendicular to the loading direction, leading to partly matrix failure. Upon reaching 1.54 mm of tensile displacement, the curve reached the ultimate tensile load of 452.4 kN with the severe splitting sound and the failure of multiple fiber bundles. Then the tensile load rapidly decreased and entered the failure stage. The test was stopped, and five tests were repeated. The load-displacement curve of carbon/glass hybrid rod was recorded.

4.2. Failure morphology

The fracture morphology of the carbon/glass hybrid rod under tensile load is shown in Fig. 5(a). The fracture morphology indicates that the carbon/glass hybrid rod failure due to brittle fracture. Among them, the interfaces between carbon-fiber core layer, glass-fiber winding layer, and glass-fiber coating layer were completely debonded. The glass-fiber coating layer occurred several striped cracks along the axial direction, with some glass fibers pulled out from the matrix. The shear failure of the matrix occurred near the connection, accompanied by multiple disordered transverse matrix cracks. Moreover, the glass-fiber winding layer was torn in a helical pattern, while the carbon fiber layer had no apparent damage. The above results showed that the interface was the weakest part of the carbon/glass hybrid rod.

4.3. Mechanical characteristics analysis of carbon/glass hybrid rod

The variation of von Mises stress in carbon/glass hybrid rod is shown in Fig. 6. The distribution of von Mises stress in the glass-fiber coating layer appeared ladder-like, increasing from the fixed end to the loaded end. The von Mises stress in the ±40° glass-fiber winding layer was more evenly distributed along the rod, while the stress near the loading end increased sharply. On the contrary, there was a maximum concentration of von Mises stress in the carbon-fiber core layer, decreasing from the fixed end to the

Table 1
Tensile test results of carbon/glass hybrid rod.

Number	Tensile load, kN	Tensile modulus, GPa	Failure mode
1	421.5	110.4	Rod spliting
2	432.2	137.1	Rod fracture at the center
3	453.3	124.8	Fiber fracture at the connection
4	475.2	130.6	Rod spliting
5	479.8	136.4	Rod fracture at the center
Average	452.4	142.1	–

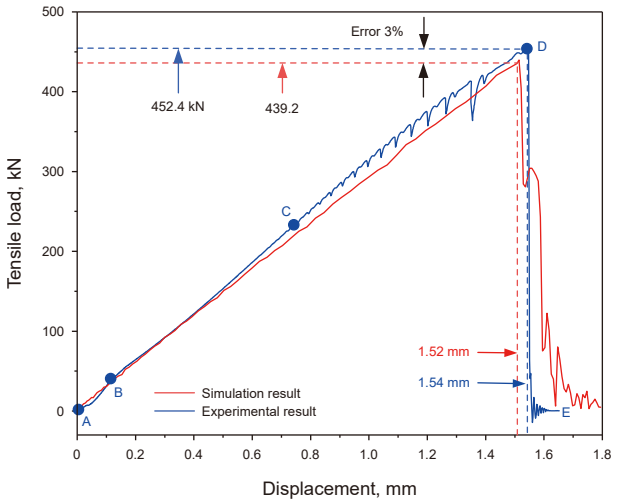

Fig. 4. Load-displacement of carbon/glass hybrid rod.

loading end. This is because the tensile load acted on the outer surface of the glass fiber coating layer and was transferred through the interface to the carbon-fiber layer. Because the carbon fiber layer has a much higher elastic modulus than the glass fiber layer, causing relative deformation between the two layers at the loading end, which results in small amplitude bonding slip at the interface leading to the release of von Mises stress in the carbon fiber layer at the loading end.

The distribution curve of von Mises stress along the axial direction of the carbon/glass hybrid rod is shown in Fig. 7. As can be seen from the figure, for glass-fiber coating layer, when the displacement was 0.3 mm, the von Mises stress remained stable at approximately 60 MPa near the axial distance of 0–150 mm, and rapidly increased to 96.4 MPa at the axial distance of 175–200 mm with an increase of 60.7%. From 0.3 mm to 0.7 mm, the von Mises concentration near the loading end was obvious, and the maximum stress increased to 164.0 and 229.6 MPa, respectively. For the −40° glass-fiber winding layer, the von Mises stress showed an uneven "double peak" distribution along the axial direction. At the axial distance of 0–150 mm from the rod, the von Mises stress remained stable at around 26.2 MPa. However, near the loading end, the von Mises stress rapidly rose to 62.2 MPa, reaching 64% of the maximum stress in the glass-fiber cladding layer. The reduction of the stress difference was due to the interface bonding force to be overcome when the external load passed from the glass-fiber coating layer to the winding layer. With the displacement increasing to 0.7 mm, the von Mises stress near the loading end of the −40° winding layer increased significantly, and the maximum stress linearly rose to 141.6 MPa. Similarly, for 40° glass-fiber winding layer, the maximum stress was 43.6 MPa at the displacement of 0.3 mm. With the displacement increasing to 0.7 mm, the maximum stress near the loading end sharply increased, which linearly increased to 111.1 MPa. For carbon fiber layer, as the displacement was 0.3 mm, the von Mises stress remained constant at 199.2 MPa along the axial distance of 0~150 mm. The von Mises stress rapidly decreased near the loading end of 150~180 mm. With the axial displacement increased to 0.7 mm, the maximum stress was linearly increased to 472.4 MPa, representing a 135.9% increase.

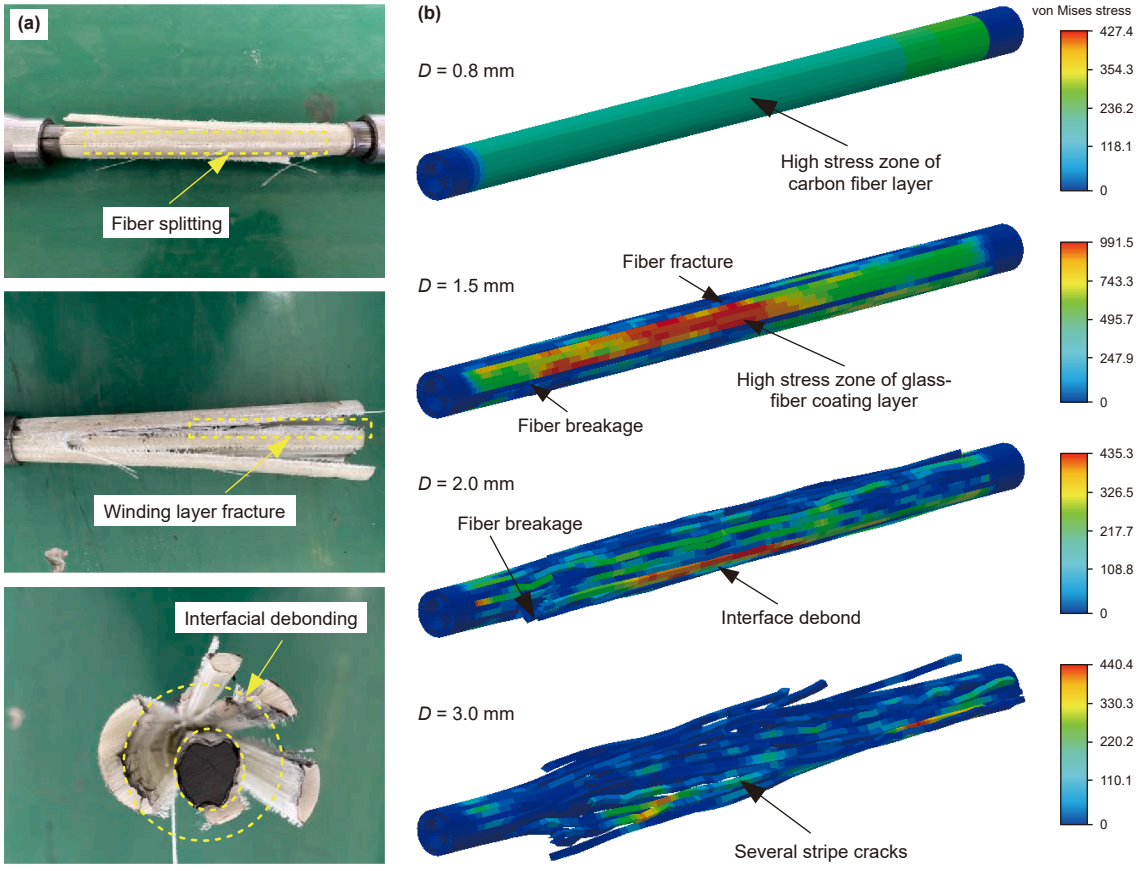

Fig. 5. Failure morphology and progressive damage failure process of carbon/glass hybrid rod with **(a)** failure morphology and **(b)** numerical failure progress.

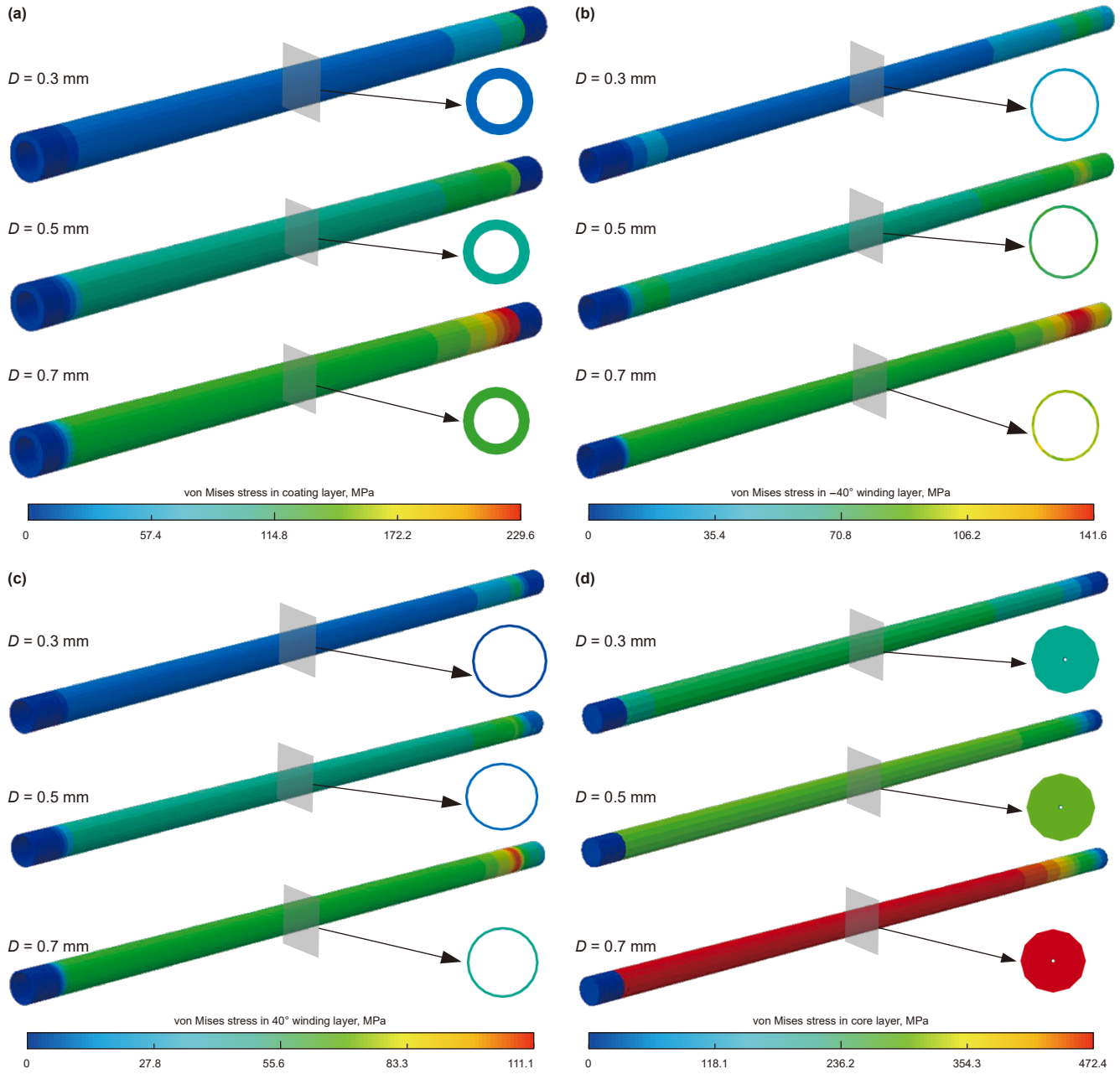

Fig. 6. The distribution of von stress in carbon/glass hybrid rod under different tensile displacements with **(a)** glass-fiber coating layer, **(b)** –40° glass-fiber winding layer, **(c)** 40° glass-fiber winding layer and **(d)** carbon-fiber layer.

5. Progressive damage analysis

5.1. Stress distribution law

The progressive damage cloud diagram of carbon/glass hybrid rod is shown in Fig. 5(b). It can be seen that at displacement of 0.8 mm, the corresponding tensile load reached 223.7 kN, which is 50% of the ultimate load (point B in Fig. 4). The load-displacement curve moved from the linear stage to the fluctuating stage. As the tensile displacement increased to 1.5 mm, the tensile load reached the limited load 439.2 kN (point C) and von Mises stress on each layer of the carbon/glass hybrid rod rapidly increased. The maximum stress in the glass-fiber coating layer was 991.5 MPa. When the tensile displacement reached to 2.0 mm, the glass-fiber coating layer experienced multi-point splitting along the circumferential direction. The cracks spread along the fiber direction and pass through the glass-fiber coating layer to the carbon fiber layer. The stored elastic energy in cracks was rapidly released, causing the von Mises stress to decrease quickly to 435.3 MPa. When the tensile displacement exceeded 3.0 mm, the maximum stress decreased slightly, and the micro-cracks propagated along the interface with intensified longitudinal splitting. The carbon/glass hybrid rod eventually experienced filament splitting.

5.2. Interfacial debonding mechanism

An analysis of the interface damage evolution law under tensile displacement of 0.8, 1.5, 1.7, and 2.0 mm was conducted in order to investigate the sliding mechanism of carbon/glass hybrid rod as

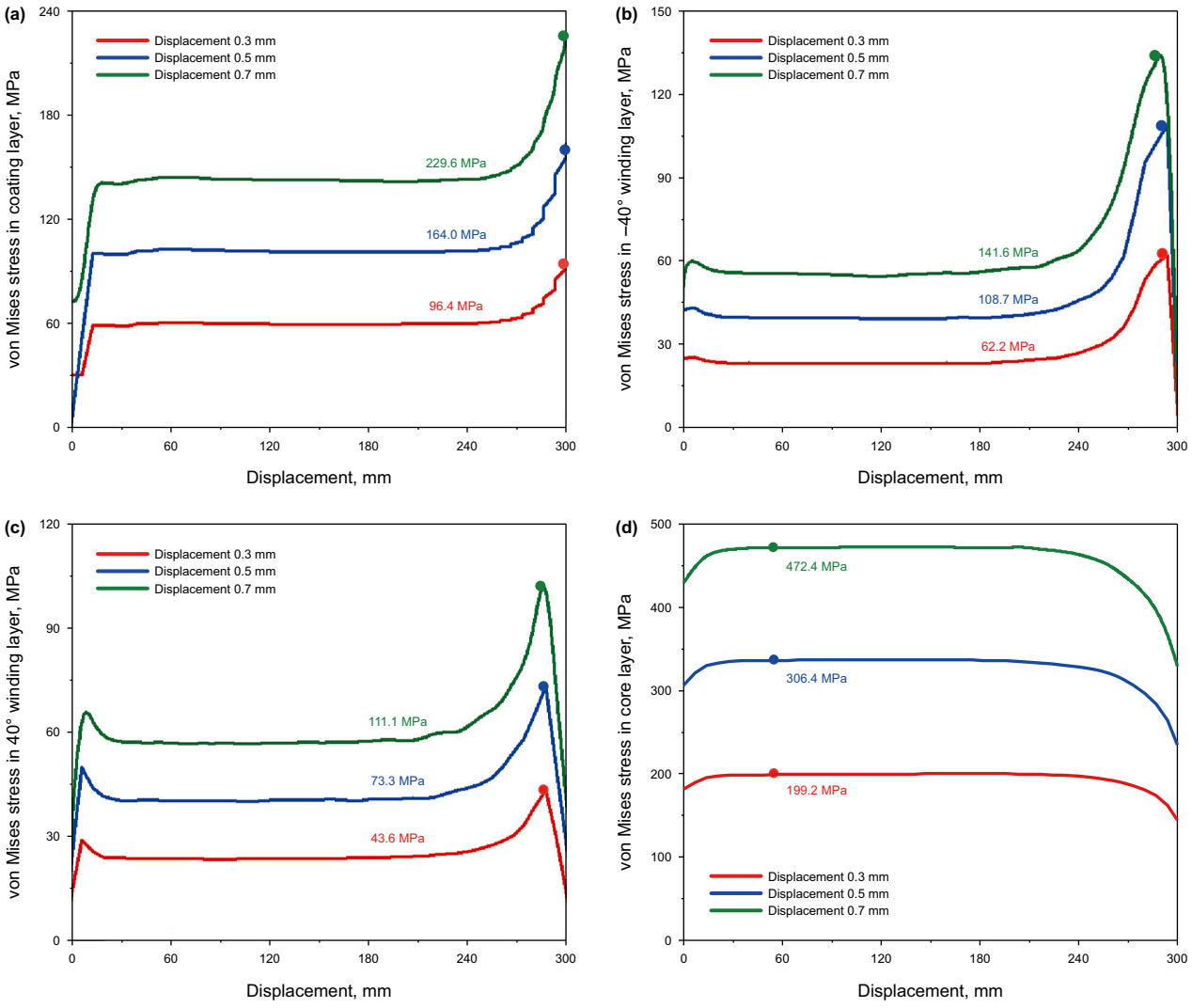

Fig. 7. The distribution curve of von Mises stress along the axial direction of the carbon/glass hybrid rod with **(a)** glass-fiber coating layer, **(b)** −40° glass-fiber winding layer, **(c)** 40° glass-fiber winding layer and **(d)** carbon fiber layer.

seen in Fig. 8. To quantify the degree of interface slide, the interface slip factor was introduced, where 1.0 represents interface slip and 0 indicates no damage at the interface.

At the loading displacement of 0.8 mm, the tensile stress was lower than the interface shear strength of the carbon/glass hybrid rod. The loading end of the rod experienced minor amplitude damage without interface slip. Among them, the −40° winding layer/coating layer exhibited the highest interface damage degree with a slip factor of 0.64. At the tensile displacement of 1.5 mm, the interfacial shear stress maintained a critical equilibrium with the interfacial shear strength of the carbon/glass hybrid rod. The interfacial shear stress in the core layer, winding layer and coating layers grew quickly at the loading end and a small area of interface slip appeared at the loading end of the interface. At a loading displacement of 1.7 mm, the sliding path of all interface increased rapidly to the fixed end. When the loading displacement approached 2.0 mm, the interface glide path almost aligns with the rod and the interface of carbon/glass hybrid rod almost completely separated.

To investigate the microscopic failure mechanism of carbon/glass hybrid rod, the fracture was observed by SEM shown in Fig. 9(a). For macro-scale debonding, when an external load was applied to the carbon/glass hybrid rod, considering the elastic modulus of glass-fiber layer is lower than that of carbon-fiber layer, inconsistent deformation easily leads to local stress concentration at the interface between carbon-fiber layer and glass-fiber layer. When the stress exceeded the interfacial strength, interfacial shear slip occurred, accompanied by interface debonding with a small part of interface hole failure. For micro-scale destocking, complex strain was initially generated within the epoxy resin and then transferred to the fiber through the epoxy/fiber interface. The elastic modulus of the epoxy resin is smaller than that of the fiber, leading to inconsistent deformation of the fiber and epoxy resin, which results in local stress concentration at the interface. When the stress exceeded the strength of the fiber/epoxy resin interface, the interface was prone to debonding and the formation of holes.

5.3. Fiber fracture mechanism

To investigate the fiber fracture mechanism in carbon/glass hybrid rod, the development law of fiber fracture factor under tensile displacement of 0.8, 1.5, and 2.0 mm was examined as seen in Fig. 10. Among them, a value of 0 with fiber fracture factor

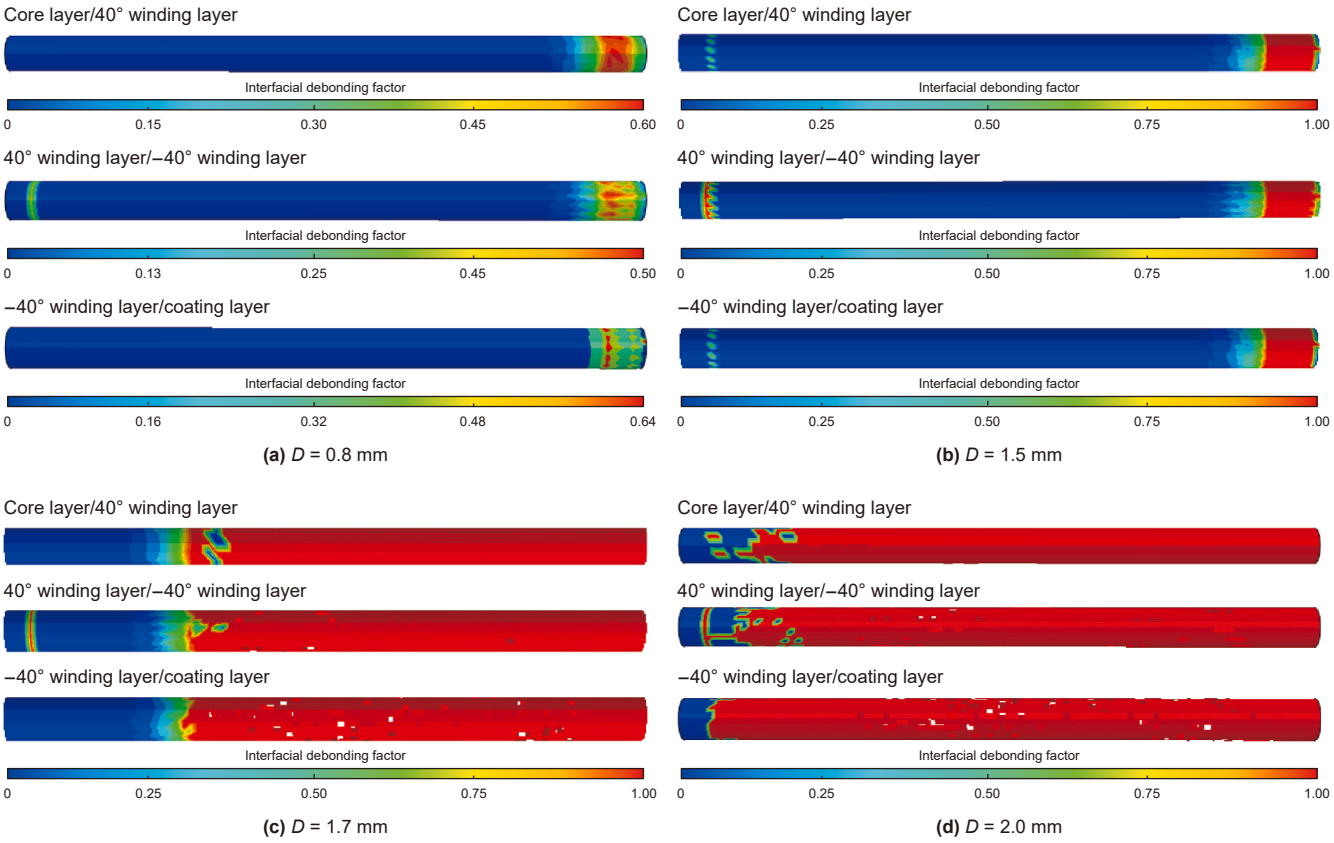

Fig. 8. Interface failure cloud image of carbon/glass hybrid rod.

indicated no fiber damage, and a value of 1.0 indicated fiber fracture.

When the tensile displacement is 0.8 mm, the fibers in the ±40° wound layer have serious tensile damage, and the tensile fracture factor is concentrated at the loading end. The peak fracture factor in the −40° wound layer and 40° wound layer is 0.28 and 0.25, respectively, while the fiber extrusion factor is almost 0. This is because the current shear stress is less than the interfacial shear strength, and the layers are stretched synchronously without extrusion deformation. Due to the small range of interface damage at the loading end, the effect of interface transfer load is weakened, and the stress is concentrated in the wound layer, resulting in tensile damage of the fibers in the wound layer.

When the tensile displacement is 1.5 mm, the peak tensile fiber fracture factor in the carbon fiber core layer, 40° wound layer and −40° wound layer is 0.68, 0.58 and 0.70, respectively, and the fracture factor of the cladding layer rapidly increases to 0.68. At the same time, fiber extrusion damage occurred at the loading end of the ±40° winding layer and the carbon fiber core layer, while there was no fiber extrusion damage in the cladding layer. This is due to the aggravation of the tensile damage of each fiber layer as the tensile displacement increases to 1.5 mm. A small range of interface slippage occurs in the interface layer near the loading end, which reduces the load transfer effect at this position, resulting in partial tensile load acting on the cladding layer, and aggravates the fiber damage degree of the cladding layer. At the same time, the shear slip of the interface makes the fibers in the winding layer and the core layer lose constraint and rebound, resulting in fiber extrusion damage.

At a tensile displacement of 2.0 mm, the fiber in the cladding layer experiences increasing damage, whereas the winding layer and core layer show minimal changes in amplitude. The reason for this is that the tensile force at this point is greater than the strength of the interface between the rod. As a result, the interface starts to slip towards the fixed end, causing a rapid decrease in the transfer of load. This leads to a concentration of the tensile force on the cladding layer. Consequently, the fibers in the cladding layer experience extensive tensile fractures over a large area. At the moment of fiber splitting, the fibers rebound towards both the fixed end and the loading end. Fiber compression damage was seen at both the loading end and the fixed end of the cladding layer.

The fiber micro fracture morphology is illustrated in Fig. 9(b)–(c). In the case of carbon fiber, the external force is applied to the epoxy resin and then transmitted to the carbon fiber through the interface. A little quantity of carbon fiber is extracted from the core layer, and the epoxy resin and carbon fiber are firmly bonded, suggesting a rather strong interface strength between the carbon fiber and resin layers. As the tensile load increases, the stress at the carbon fiber/epoxy resin interface cannot be relieved, resulting in increased tensile energy exerted on the carbon fiber. When the stress surpasses the strength threshold of the carbon fiber, the carbon fiber will undergo brittle fracture along the 45° direction of the shear force. As a result, the load will shift from the fractured fiber to the adjacent fiber, leading to the fracture of the surrounding fiber. In comparison to carbon fiber, glass fiber exhibits reduced bonding strength with epoxy resin. This results in a significant amount of glass fiber being extracted from the resin matrix. The surface of glass fiber is smooth, with just a minimal amount of resin adhering to it. The weak interface between the glass fiber surface and the epoxy resin causes stress relaxation at the glass fiber/epoxy resin interface. This leads to ineffective

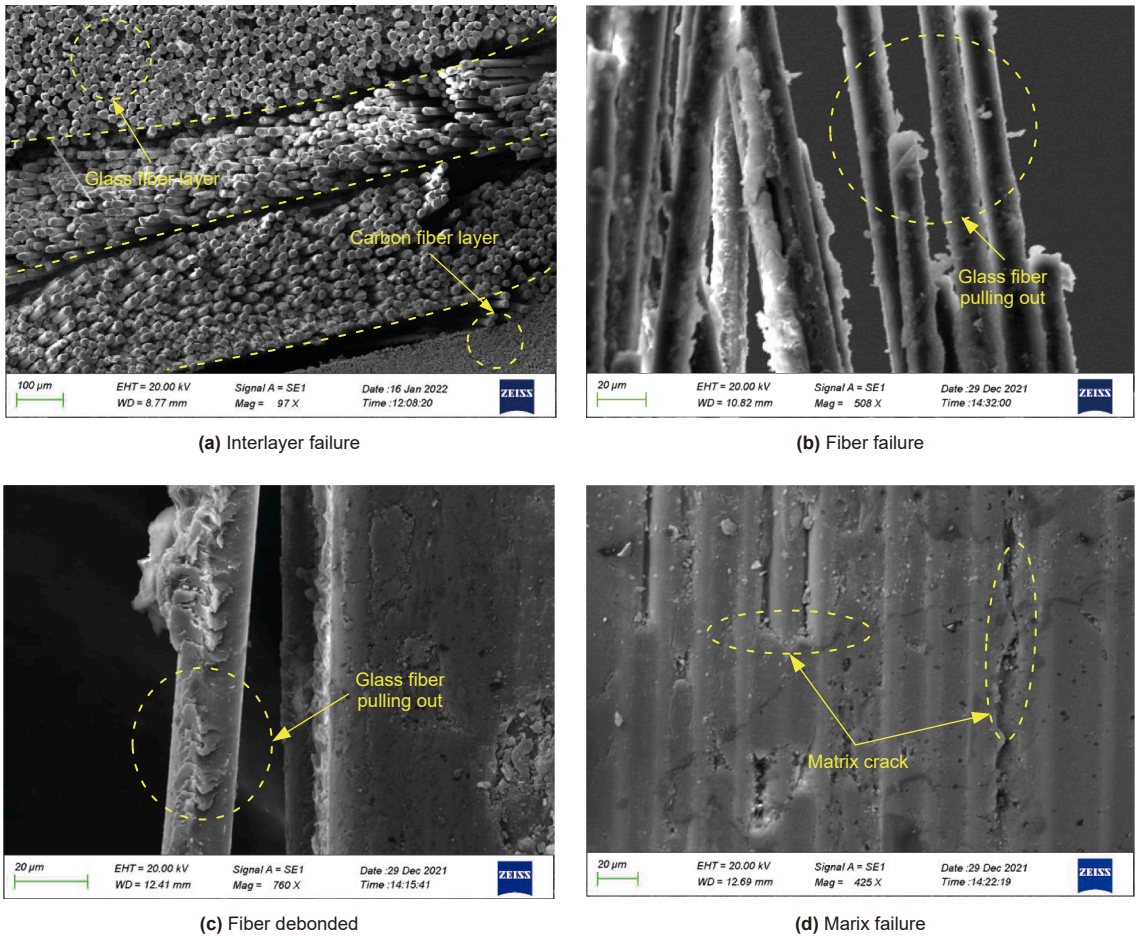

Fig. 9. The damage microstructure of interface in carbon/glass hybrid rod.

transmission of stress to the glass fiber, resulting in interface stripping between the glass fiber and the matrix.

5.4. Matrix fracture mechanism

To investigate the matrix fracture mechanism in carbon/glass hybrid rod, the development law of matrix fracture factor under tensile displacement of 0.8, 1.5, and 2.0 mm was examined as seen in Fig. 11. Among them, a value of 0 with matrix fracture factor indicated no matrix damage, and a value of 1.0 indicated matrix fracture.

At a tensile displacement of 0.8 mm, the distribution pattern of matrix cracking factors in each layer aligns with that of fiber tensile fracture factors. Among them, the severe matrix cracking damage is seen in the ±40° winding layer, where it is steady at axial positions of 0–225 mm and rapidly increases to 0.95 at 225–300 mm. The matrix in both the core layer and the coating layer exhibits minimal degradation. This is because, once the fibers in the wound layer are destroyed, the residual load is transferred from the fibers to the matrix, causing the matrix in wound layer to be damaged first. At the same time, the damage caused by matrix extrusion was not easily detectable, and the highest factor of matrix extrusion was 0.14, occurring at the winding layer of 40°.

At a tensile displacement of 1.5 mm, the wound layer experiences matrix cracking and matrix extrusion. In the core layer, matrix cracking and matrix extrusion damage occur within a limited area. The peak cracking factor is measured at 0.81. Additionally, the coating layer shows partial matrix cracking and matrix extrusion damage at the loading end, with a peak matrix cracking factor of 0.19. As the tensile displacement reaches 2.0 mm, the fiber in the cladding layer experiences increased tensile fracture, leading to the formation of cracks and extrusion in the glass fiber cladding layer. As the tensile displacement reaches 2.0 mm, the fracture of the fiber in the cladding layer becomes more severe, leading to the formation of cracks and extrusion in the glass fiber cladding layer.

The microscopic damage diagram of the matrix in the carbon/glass hybrid rod is shown in Fig. 9(d). Following the breakage of the fiber, the stress is transported back to the matrix via the fiber interface due to the presence of residual tensile load. Due to the low strength of the epoxy resin substance, the matrix is susceptible to shear failure, resulting in the formation of micro-cracks that are oriented perpendicular to the greatest primary stress. The matrix exhibits a wavy micro-structure and contains several discontinuous voids. This occurs during the curing process as a result of the disparate expansion coefficients between the fiber and matrix resin, as well as the repulsion of gas molecules, leading to the formation of pores. Consequently, the load transfer performance is compromised, and damage expansion parallel to the fiber direction becomes more likely. This leads to fluctuations in the load-displacement curve and a decrease in mechanical property stability, ultimately resulting in longitudinal splitting and subsequent damage.

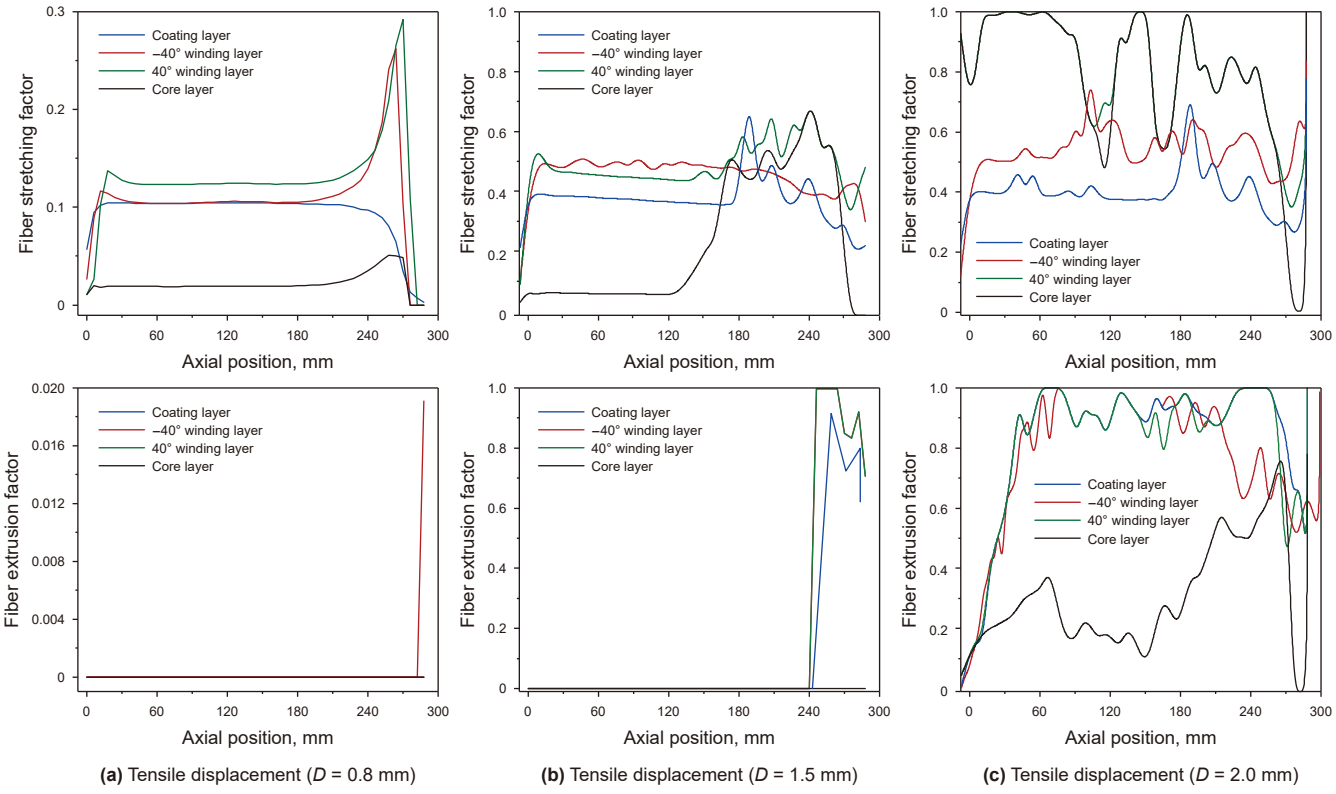

Fig. 10. The fiber and matrix failure cloud image of carbon/glass hybrid rod at 2.0 mm tensile displacement.

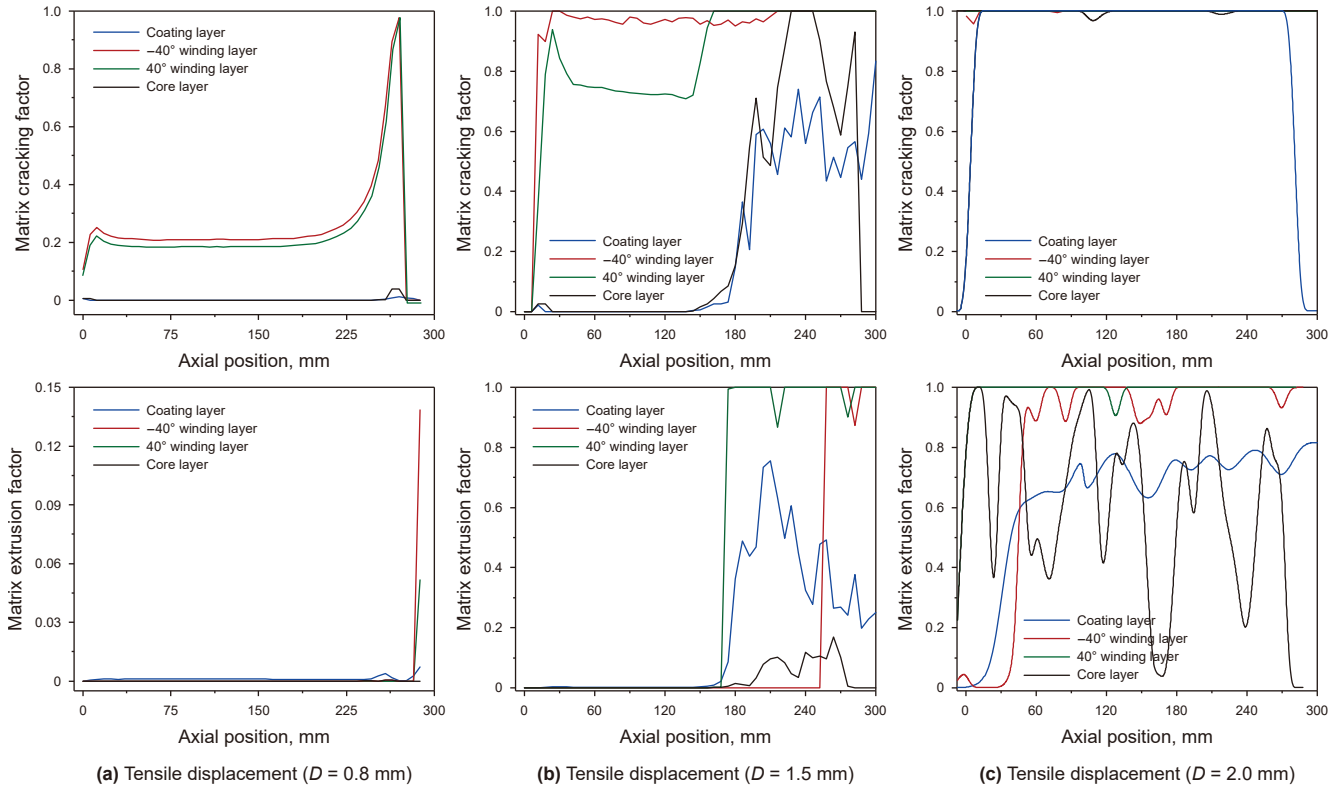

Fig. 11. The fiber and matrix failure cloud image of carbon/glass hybrid rod at 2.0 mm tensile displacement.

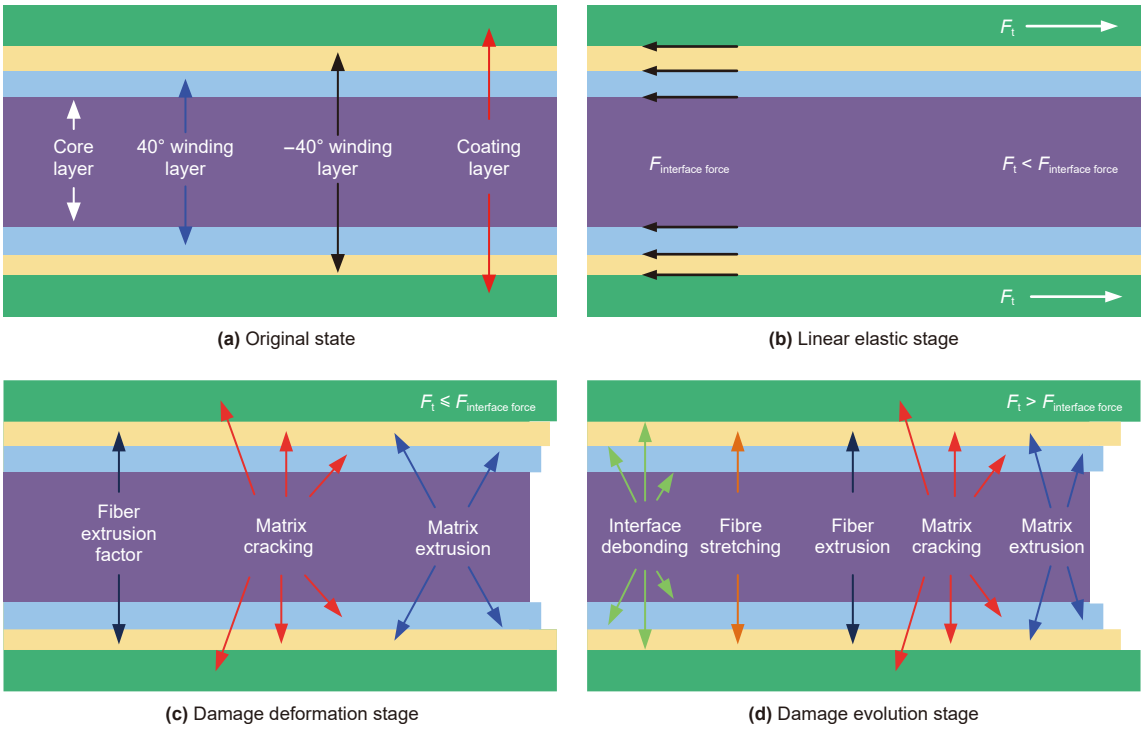

Fig. 12. The damage mechanism of the carbon/glass hybrid rod when subjected to tensile load.

5.5. Solution of issues

In summary, the damage mechanism of the carbon/glass hybrid rod when subjected to tensile load is illustrated in Fig. 12. The damage mechanism includes:

(1) While the tensile displacement ranged from 0 to 0.8 mm, the rod remains in a state of linear elastic deformation and has not experienced any failure. Because the tensile load at this stage is less than the interfacial shear force. As a result, the tensile stress is applied to the cladding layer and then transferred to the carbon fiber core layer through the winding layer. This process causes deformation in each layer of the rod. Due to the higher elastic modulus of carbon fiber compared to glass fiber, the deformation of the cladding layer and winding layer aligns with that of the carbon fiber core layer.

(2) When the tensile displacement ranges from 0.8 mm to 1.5 mm, the rod enters the damage deformation stage. The layers are unable to be deformed synchronously under the same load due to the higher elastic modulus of carbon fiber than that of glass fiber. Consequently, the shear stress at the carbon/glass interface and the concentration at the loading end increase. The interface at the loading end of the rod experiences a small area slip, and the effect of the interface transfer load is diminished when the shear stress exceeds the interface shear strength at this location. The rod sustained fiber tensile damage, matrix cracking damage, fiber extrusion fracture, and matrix extrusion fracture. The tensile load and the interfacial shear force achieve critical equilibrium when the tensile displacement reaches 1.5 mm, and the corresponding load reaches the peak tensile load.

(3) When the tensile displacement exceeds 1.5 mm, the rod enters the damage evolution stage. The winding layer in the middle position is severely damaged, and the effect of the interface transfer load is rapidly weakened, resulting in a concentrated tensile load on the cladding layer. This is due to the fact that the tensile load at this stage is greater than the interfacial shear force of the rod, which causes a large area of shear slip at the interface of the cladding layer/carbon fiber core layer. The compression damage of the fibers and the matrix is the result of the fibers bouncing back to the fixed end and the loading end when the cladding layer separates due to internal stress. Interface debonding, matrix cracking, matrix extrusion, fiber extrusion fracture, and fiber tensile fracture are the primary damage modes of carbon/glass hybrid rods at this stage.

In conclusion, the interlayer hybrid structure of the carbon/glass composite rod that is currently employed in oil fields. In accordance with the rod fracture mechanism, the interface slip between the rod layers is highly susceptible to occurrence due to the low interface strength and asynchronous deformation of the interface between the carbon-fiber core layer and the glass-fiber cladding layer. This results in the initial failure of the winding layer and the rapid weakening of the interface load transfer effect. Ultimately, the rod experiences interlayer fracturing failure. Consequently, the primary factor in enhancing the tensile strength of a carbon/glass hybrid rod is the prevention of interlayer fracturing.

6. Conclusions

The strength prediction model of a carbon/glass hybrid rod was constructed using the constitutive model of multi-mode damage. The accuracy of the simulation model was confirmed through tensile tests. The distribution features were determined and the damage mechanisms were identified, explaining the reason of rod

failure on site and offering guidance for enhancing the strength of carbon/glass hybrid rods. The main conclusions are as follows:

(1) The failure process of carbon/glass hybrid rod was divided into four stages: fixture pre-tightening, linear elastic, damage evolution and failure splitting. The average experimental tensile load was 452.4 kN. The fracture morphology indicates that the carbon/glass hybrid rod failure due to brittle fracture, and the interfaces were completely debonded.
(2) The simulation model calculated the ultimate tensile load as 439.2 kN, with a corresponding axial displacement of 1.52 mm. The discrepancy between the test results and the simulation results was 3%, resulting from the initial asymmetrical error of the test model and the installation error of the test fixture.
(3) According to the linear elastic stage, with the displacement increasing from 0.3 mm to 0.7 mm, the maximum von Mises stress in glass-fiber coating layer, −40° glass-fiber winding layer, 40° glass-fiber winding layer and carbon fiber layer, increased from 96.4, 62.2, 43.6 and 199.2 MPa to 229.6, 141.6, 111.1 and 472.4 MPa, respectively.
(4) At a tensile displacement of 0.8 mm, the carbon/glass hybrid rod exhibited damage in the form of small matrix breaking. At a tensile displacement of 1.5 mm, the failure mode observed was a combination of matrix cracking and fiber fracture damage. The extent of damage in terms of matrix extrusion and fiber extrusion was quite little. At a tensile displacement of 2.0 mm, the primary damage mechanisms observed include interface debonding failure, matrix cracking failure, matrix extrusion failure, fiber extrusion damage, and fiber fracture damage.

CRediT authorship contribution statement

Yan-Wen Zhang: Writing – original draft. **Yu-Jing Chen:** Funding acquisition. **Jia-Qi Che:** Writing – review & editing. **Yu-Feng Jiang:** Software. **Wen-Cheng Liu:** Conceptualization. **Xin-Fu Liu:** Resources.

Declaration of interest statement

We declare that we have no financial and personal relationships with other people or organizations that can inappropriately influence our work, there is no professional or other personal interest of any nature or kind in any product, service and/or company that could be construed as influencing the position presented in, or the review of, the manuscript entitled.

Acknowledgements

The China Postdoctoral Science Foundation (GZB20250682, 2025M770294, and 2025T180077) are sincerely acknowledged. The Shandong Provincial Natural Science Fund for Excellent Young Scientists Fund Program (Overseas) (2025HWYQ-030) is gratefully acknowledged. The support from the Taishan Young Scholar Expert Program of Shandong Province (TSQN202408083) is sincerely acknowledged. The Postdoctoral Innovation Project of Shandong Province (SDCX-ZG-202503048), Qingdao Postdoctoral Science Foundation (QDBSH20250102256), Independent Innovation Research Program Project of China University of Petroleum (East China) (24CX06010A) and the Fundamental Research Funds for the Central Universities (202513039) are also thanked.

References

Akpinar, S., Aydin, M., 2014. 3-D non-linear stress analysis on the adhesively bonded composite joint under bending moment. Int. J. Mech. Sci. 81, 149–157. https://doi.org/10.1016/j.ijmecsci.2014.02.024.
Al-Mahfooz, M., Mahdi, E., 2023. Bending behavior of glass fiber reinforced composite overwrapping PVC plastic pipes. Compos. Struct. 251. https://doi.org/10.1016/j.compstruct.2023.115421.
Bai, J., Seeleuthner, P., Bompard, P., 1997. Mechanical behaviour of ±55° filament-wound glass-fibre/epoxy-resin tubes: I. Microstructural analyses, mechanical behaviour and damage mechanisms of composite tubes under pure tensile loading, pure internal pressure, and combined loading. Compos. Sci. Technol. 57 (2), 141–153. https://doi.org/10.1016/S0266-3538(96)00135-7.
Bek, L., Kottner, R., Laš, V., 2021. Material model for simulation of progressive damage of composite materials using 3D Puck failure criterion. Compos. Struct. 259, 113435. https://doi.org/10.1016/j.compstruct.2021.113435.
Betts, D., Sadeghian, P., Fam, A., 2019. Investigation of the stress-strain constitutive behavior of ±55° filament wound GFRP pipes in compression and tension. Compos. Part B Eng. 172, 243–252. https://doi.org/10.1016/j.compositesb.2019.05.036.
Biscaia, H., Borba, I., Silva, C., et al., 2016. A nonlinear analytical model to predict the full-range debonding process of FRP-to-parent material interfaces free of any mechanical anchorage devices. Compos. Struct. 138, 52–63. https://doi.org/10.1016/j.compstruct.2015.11.030.
Cox, K., Menshykova, M., Menshykov, O., et al., 2019. Analysis of flexible composites for coiled tubing applications. Compos. Struct. 225, 111164. https://doi.org/10.1016/j.compstruct.2019.111164.
Delmonte, J., 1987. Properties of Carbon/Graphite Composites. Krieger Publishing Co., Huntington.
Doitrand, A., Fagiano, C., Chiaruttini, V., et al., 2015. Experimental characterization and numerical modeling of damage at the mesoscopic scale of woven polymer matrix composites under quasi-static tensile loading. Compos. Sci. Technol. 119, 1–11. https://doi.org/10.1016/j.compscitech.2015.08.012.
Du, J., Zhang, D., Zhang, Y., et al., 2024. Design and comparative analysis of alternative mooring systems for offshore floating photovoltaics arrays in ultra-shallow water with significant tidal range. Ocean Eng. 302, 117649. https://doi.org/10.1016/j.oceaneng.2024.117649.
Feng, D., Qi, Y., Yu, Y., et al., 2021. Tensile properties of marine fiber reinforced composite flexible pipes. J. China Univ. Pet. (Ed. Nat. Sci.) 45 (4), 146–152. https://doi.org/10.3969/j.issn.1673-5005.2021.04.017.
Firouzsalari, S.E., Dizhur, D., Jayaraman, K., et al., 2021. Bending behaviour of flax fabric-reinforced epoxy pipes. Compos. Part A Appl. Sci. Manuf. 140, 106179. https://doi.org/10.1016/j.compositesa.2020.106179.
Hasheminia, S., Park, B., Chun, H., et al., 2019. Failure mechanism of bonded joints with similar and dissimilar material. Compos. Part B Eng. 161, 702–709. https://doi.org/10.1016/j.compositesb.2019.07.005.
Hou, Y., Wang, W., Meng, L., et al., 2022. An insight into the mechanical behavior of adhesively bonded plain-woven-composite joints using multiscale modeling. Int. J. Mech. Sci. 219, 107063. https://doi.org/10.1016/j.ijmecsci.2022.107063.
Karthik, K., Prakash, J.U., Binoj, J.S., et al., 2022. Effect of stacking sequence and silicon carbide nanoparticles on properties of carbon/glass/Kevlar fiber reinforced hybrid polymer composites. Polym. Compos. 43 (9), 6096–6105. https://doi.org/10.1002/pc.2605.
Kupski, J., de Freitas, S.T., Zarouchas, D., et al., 2019. Composite layup effect on the failure mechanism of single lap bonded joints. Compos. Struct. 217, 14–26. https://doi.org/10.1016/j.compstruct.2019.03.062.
Malmorad, M., Rahmani, K., Sarfaraz, R., 2020. Experimental investigation and modeling of temperature-dependent flexural strength of hybrid composite rods. Mech. Mater. 150 (3), 103572. https://doi.org/10.1016/j.mechmat.2020.103572.
Menshykova, M., Guz, I.A., 2014. Stress analysis of layered thick-walled composite pipes subjected to bending loading. Int. J. Mech. Sci. 88, 289–299. https://doi.org/10.1016/j.ijmecsci.2014.07.008.
Qi, Y., Cai, C., Sun, P., et al., 2023. Crude oil cracking in deep reservoirs: a review of the controlling factors and estimation methods. Pet. Sci. 20 (4), 1978–1997. https://doi.org/10.1007/s12182-023-00950-7.
Wang, Y., Hu, Y., Zhang, K., et al., 2025. The impact of filament winding configurations on the ultimate load-bearing capacity of non-metallic flexible composites. Ocean Eng. 341, 122516. https://doi.org/10.1016/j.oceaneng.2025.122516.
Xian, G., Niu, Y., Qi, X., et al., 2024. Water absorption and property evolution of epoxy resin under hygrothermal environment. J. Mater. Res. Technol. 31, 3982–3997. https://doi.org/10.1016/j.jmrt.2024.12.026.
Yan, X., Cao, S., 2018. Structure and interfacial shear strength of polypropylene-glass fiber/carbon fiber hybrid composites fabricated by direct fiber feeding injection molding. Compos. Struct. 185, 362–372. https://doi.org/10.1016/j.compstruct.2017.11.030.
Zhang, Y., Che, J., Wang, H., et al., 2024a. Mechanics behavior and failure mechanism of the intralayer carbon/glass hybrid rod. Polym. Compos. 45 (8), 7586–7601. https://doi.org/10.1002/pc.28290.
Zhang, Y., Che, J., Zhang, H., et al., 2024b. An evaluation of the influence of mechanical strength on carbon/glass hybrid rods under various design parameters. Geoenergy Sci. Eng. 240, 212927. https://doi.org/10.1016/j.geoen.2024.212927.
Zhang, Y., Wang, S., Xu, M., et al., 2026. Anchoring behaviors and optimization of mechanical-bonding joint for FRP tendon. Ocean Eng. 349, 124149. https://doi.org/10.1016/j.oceaneng.2025.124149.